Mars upper atmospheric responses to the 10 September 2017 solar flare: A global, time-dependent simulation

Xiaohua Fang [1], David Pawlowski [2], Yingjuan Ma [3], Stephen Bougher [4], Edward Thiemann [1], Francis Eparvier [1], Wenbin Wang [5], Chuanfei Dong [6], Christina O. Lee [7], Yaxue Dong [1], Mehdi Benna [8], Meredith Elrod [8], Phillip Chamberlin [1], Paul Mahaffy [8], and Bruce Jakosky [1]

[1]Laboratory for Atmospheric and Space Physics, University of Colorado, Boulder, Colorado, USA

[2]Physics and Astronomy Department, Eastern Michigan University, Ypsilanti, Michigan, USA

[3]Department of Earth, Planetary and Space Sciences, University of California, Los Angeles, California, USA

[4]Department of Climate and Space Sciences and Engineering, University of Michigan, Ann Arbor, Michigan, USA

[5]High Altitude Observatory, National Center for Atmospheric Research, Boulder, Colorado, USA

[6]Department of Astrophysical Sciences and Princeton Plasma Physics Laboratory, Princeton University, Princeton, New Jersey, USA

[7]Space Sciences Laboratory, University of California, Berkeley, California, USA

[8]NASA Goddard Space Flight Center, Greenbelt, Maryland, USA

Key Points:

- Ionospheric perturbation follows the flare in time and is concentrated mostly below 110 km altitude.
- Neutral atmospheric perturbation increases with altitude and is important above 150 km altitude.
- It takes the neutral atmosphere 2.5 hours to reach the perturbation peak and 10 more hours to recover.

Corresponding author: Xiaohua Fang, Xiaohua.Fang@lasp.colorado.edu

Abstract

We report the first global, time-dependent simulation of the Mars upper atmospheric responses to a realistic solar flare event, an X8.2 eruption on 10 September 2017. The Mars Global Ionosphere-Thermosphere Model runs with realistically specified flare irradiance, giving results in reasonably good agreement with the Mars Atmosphere and Volatile EvolutioN spacecraft measurements. It is found that the ionized and neutral regimes of the upper atmosphere are significantly disturbed by the flare but react differently. The ionospheric electron density enhancement is concentrated below ∼110 km altitude due to enhanced solar X-rays, closely following the time evolution of the flare. The neutral atmospheric perturbation increases with altitude and is important above ∼150 km altitude, in association with atmospheric upwelling driven by solar EUV heating. It takes ∼2.5 hours past the flare peak to reach the maximum disturbance, and then additional ∼10 hours to generally settle down to pre-flare levels.

1 Introduction

Solar flares represent an important type of space weather event, in which a tremendous amount of energy is released into the heliosphere in the form of radiation bursts and hence imposes significant disturbances upon planetary atmospheres. With dramatic perturbations on solar irradiance, solar flares offer an invaluable opportunity to test our understanding and constrain first-principles modeling of how solar ionizing and heating fluxes dissipate and redistribute the energy in atmospheric and ionospheric systems. An accurate description of upper atmospheric processes is critical not only for understanding the higher-altitude plasma environment and atmospheric loss by solar wind stripping, but also for the safety of current and future Mars orbital platforms.

While there have been numerous studies on the effectiveness of solar flares at Mars, nearly all of them focus on ionospheric responses [*Gurnett et al.*, 2005; *Nielsen et al.*, 2006; *Mendillio et al.*, 2006; *Haider et al.*, 2009; *Mahajan et al.*, 2009; *Lollo et al.*, 2012; *Haider et al.*, 2012; *Fallows et al.*, 2015] and little is known about the thermospheric impact of solar flares [e.g., *Thiemann et al.*, 2015]. Historically, the main challenge in the study of the Mars upper atmosphere has been the lack of systematic and comprehensive neutral species observations except for limited knowledge derived from sparse aerobraking activities [e.g., *Bougher et al.*, 2000, and references therein]. Moreover, there has been

a lack of solar irradiance measurements at the Mars' orbit until the NASA Mars Atmo-
sphere and Volatile EvolutioN (MAVEN) mission [*Jakosky et al.*, 2015], which for the first
time carries both solar extreme ultraviolet (EUV) and neutral particle detectors, suitable
for solving the cause-and-effect connection between the Sun and Mars. Different from pre-
vious unpublished conference presentations performing generic model runs for solar flares,
in this study we make the first numerical attempt to quantify global perturbations of the
Martian upper atmosphere in response to a real solar flare event using realistic flare irradi-
ance, and to make direct model-data comparisons for the flare effects.

2 The 10 September 2017 Solar Flare Irradiance at Mars

On 10 September 2017, one of the most powerful solar flares in the recent decade
erupted from the solar active region AR2673 and impacted Mars. The activities from
AR2673 also include an eruption of a fast and wide coronal mass ejection (see *Lee et al.*
[2018] for an overview). The X8.2-class solar flare eruption manifests itself in dramatic
enhancement over a broad wavelength range including X-ray and EUV. It has been found
by terrestrial solar flare studies that thermospheric responses are more dependent on time-
integrated energy inputs than on peak irradiance fluxes [e.g., *Pawlowski and Ridley*, 2008,
2011]. Therefore, to yield a reasonable assessment of the flare effectiveness in the Martian
upper atmosphere, we need not only a detailed description of the flare irradiance spectra
but also their evolution with time during the event. There is also a need for extrapolating
direct solar irradiance measurements by the MAVEN EUV Monitor (EUVM) within three
discrete finite-wavelength channels (0.1-7 nm, 17-22 nm, and 121-122 nm, see *Eparvier
et al.* [2015]) to a broad radiation range that is of importance to atmospheric absorption.
Because of an especially high solar corona temperature associated with this specific flare,
we adopt the ad-hoc, physics-based spectral irradiance model of *Thiemann et al.* [2018]
to construct the time-varying solar irradiance during the event (see supporing informa-
tion of this paper for more details). Flare irradiance observations at Earth and photoelec-
tron observations at Mars have indicated that the spectra used here are an improvement
over the EUVM Level 3 (L3) spectra [*Xu et al.*, 2018]. It has been speculated that the er-
ror/uncertainty of the spectral irradiance model for this study is better than that of the L3
model, whose upper limit is about 40% [*Thiemann et al.*, 2017].

3 Numerical Simulation of Upper Atmospheric Effects

The Mars Global Ionosphere-Thermosphere Model (MGITM) [*Bougher et al.*, 2015a,b] is adopted to investigate the solar flare impact on the Martian upper atmosphere. MGITM combines the terrestrial GITM framework of *Ridley et al.* [2006] with Mars fundamental physical parameters, ion-neutral chemistry, and key radiative processes to capture the basic observed features of the thermal, compositional, and dynamical structure of the Mars atmosphere from the ground to ~300 km altitude. In the present study, MGITM runs at a high resolution of 2.5° longitude by 2.5° latitude by 2.5-km altitude (~0.25 scale height). The time resolution of the model is about a few seconds (which is dynamically adjusted), although the model results are output every 5 minutes during the flare time period. The localized crustal magnetic field, which adds complexity to the near-Mars space environment [e.g., *Fang et al.*, 2015, 2017], is neglected. In this work, we focus more on the flare impact from a system perspective than small-scale or regional disturbances.

In order to reasonably describe the Martian thermospheric and ionospheric state changes during the space weather event, we start the MGITM run ~60 Martian solar days prior to the flare onset, assuming constant solar irradiance inputs at a pre-event level of 2017-09-03/00:00 (>7 days before the X-flare). The purpose of the preconditioning run is to spin up the global dynamics to achieve a pseudo steady state before the flare. MGITM then runs using time-varying, realistically configured solar inputs (at 1-minute time cadence) in the next 9 days from 09-03/00:00 till 09-12/00:00. Note that several relatively weak M-class solar flares happened during September 8-9 prior to the examined X-class flare. Figures 1a-1e present the abundance altitude profiles of five key neutral species (CO_2, O, CO, N_2, and Ar) retrieved from the MGITM results along three MAVEN periapsis passages. These spacecraft tracks span the pre-flare, near-post-flare, and far-post-flare phases of the event, with periapsis passage times of 09-10/08:49, 09-10/17:42, and 09-11/02:34, respectively. With an orbital period of about 4.5 hours, MAVEN missed the chance to closely observe the upper atmospheric responses during the peak of the flare event (approximately at 09-10/16:15, see the supporting information). Figures 1f-1j show the percentage changes in the neutral densities along the near-post-flare and far-post-flare periapsis passages relative to the pre-flare values at the same altitudes. The in-situ neutral measurements for comparison are from the MAVEN Neutral Gas and Ion Mass Spectrometer (NGIMS) [*Mahaffy et al.*, 2014, 2015; *Benna et al.*, 2015]. Here we use only inbound segments to exclude potential contamination on the instrument. Complementary discus-

sions of the MAVEN observations of the Martian upper atmosphere and ionosphere during this event have been given by *Elrod et al.* [2018] and *Thiemann et al.* [2018], respectively.

The model-data comparison from pre-flare to post-flare in Figures 1a-1e shows that MGITM generally captures the basic structures of the upper atmospheric density profiles along all the three examined MAVEN orbits. The model results agree reasonably well with the data for CO_2, CO, and Ar, while significant model deviation is found, including underestimation of the abundances for O (particularly below ~180 km altitude) and for N_2. The detailed examination of the atmospheric density perturbations in percent, as presented in Figures 1f-1j for both the model and data, illustrates a dramatic density enhancement in all the key neutral species during the flare and then a general recovery along the far-post-flare orbit. The MAVEN data indicate that the densities along the near-post-flare orbit (in red) increase more with increasing altitude, from by up to about 50% at altitudes lower than ~190 km to by a factor of 3 or more at higher altitudes. The model captures the increasing trend with altitude, while the great enhancement amplitude above the exobase (which is typically located at around 200 km altitude) is missed by the model. This is partly because the model is subject to more limitations in physics as neutral species gradually change from a fluid-like behavior in the thermosphere toward a ballistic motion across the exobase. Along the far-post-flare orbit (in blue), the model accurately reproduces the slight decrease in the thermospheric concentrations but misses the reversed change in the exosphere. In addition, the wave-like structures in the observations are not accounted for in the model run. Nevertheless, the comparisons as seen in Figure 1 show that our simulation reasonably captures the neutral density enhancement during the flare and the subsequent recovery, on both spatial and temporal scales. It should be pointed out that no ad hoc tuning or adjustment has been made to the MGITM model for this specific event, except for the solar irradiance specification as described before. Considering the complexity and challenging nature of modeling a global system in a time-evolving fashion, the agreement as seen in Figure 1 is remarkable and underscores the usefulness of the model in understanding of the Martian upper atmospheric behavior of the first order [*Bougher et al.*, 2015b]. While the model-data discrepancy indicates an opportunity to identify potential processes that could be improved or considered in future work (see *Bougher et al.* [2015a] for discussions of MGITM simplification and empirical approximations), the numerical study that we report here represents one of the best modeling capabilities that are currently available to the Mars upper atmospheric community.

150   The direct orbit-to-orbit comparison is straightforward but does not necessarily rep-
151 resent the true atmospheric perturbations solely due to the space weather event. The Mars
152 system is dynamic in nature and is seldom in a steady state even under quiescent solar
153 conditions. Large orbit-to-orbit variability has been reported in the Martian upper atmo-
154 sphere [*Bougher et al.*, 2015b, 2017; *Zurek et al.*, 2017]. The changes as seen from orbit
155 to orbit implicitly result from many variability sources other than the flare, including, for
156 example, longitudinal variations of atmospheric heating due to largely inhomogeneous dis-
157 tributions of thermal inertia and albedo [e.g., *Putzig et al.*, 2005]. The wide longitudinal
158 span among the orbits due to planetary rotation contributes in part to the changes shown
159 in Figure 1. To add to the complexity, the MAVEN orbital projection in the Mars-centered
160 Solar Orbital (MSO) coordinate system is also not fixed but precesses with time. In or-
161 der to reliably retrieve the thermospheric perturbations only due to the 10 September 2017
162 flare, we run a benchmark case for the non-flare scenario, similar to the approach taken
163 by the terrestrial study of *Pawlowski and Ridley* [2008]. The non-flare case runs under the
164 identical conditions over the same time frame as used in the flare case except that the so-
165 lar irradiance starting from 09-10/15:00 is held constant at the minimum post-flare level
166 during 2017-09-11. The purpose of selecting the post-flare minimum during the flare de-
167 velopment for the benchmark (non-flare) case is to ensure that the solar irradiance change
168 in the flare case is always positive in comparison with the non-flare case. A comparison
169 of these two time-varying cases enables us to quantify the net effects that the flare has on
170 the upper atmosphere and their time evolution.

171   Figure 2 describes the net flare effects in the dayside upper atmosphere. Figures 2a-
172 h give the percentage changes by subtracting the non-flare case from the flare case and
173 then dividing the difference by the non-flare case. The examined parameters in panels a-
174 h correspond to electron density, neutral temperature, neutral pressure, CO_2, O, CO, N_2
175 densities, and O/CO_2 density ratio, respectively. The altitude profiles for comparison are
176 obtained by averaging over the entire dayside for solar zenith angle (SZA) less than $90°$,
177 using corresponding horizontal areas as weights. A prominent feature as seen in Figure 2
178 is that from a system perspective, the Martian ionosphere and neutral atmosphere on aver-
179 age undergo significant increase in density and temperature and apparent decrease in the
180 mixing ratio of O relative to CO_2 in response to the solar irradiance enhancement during
181 the flare. It takes the upper atmosphere more than 12 hours past the flare peak to gener-

ally settle down to the pre-flare level. In what follows, we discuss in detail how the Mars system is disturbed.

One response difference between the upper atmospheric neutral and ionized regimes is on their temporal development: they both react instantaneously but with distinctly different time scales. The ionospheric density increase, which is the most pronounced below 110 km altitude, is closely in line with the increase in X-ray photon fluxes and thus the resulting photoionization. The short reaction time of the ionosphere is due to fast photochemical reactions. This is also seen in the negligible time delay between the artificial solar shortwave radiation bite-outs (as seen in Supporting Information Figure S1a) and brief ionospheric depletions (after ~21:55 UT and ~23:35 UT). Since these instrument effects hardly impact the atmosphere, we didn't make corrections but instead find them useful as a diagnostic of the ionospheric response. As a comparison, the atmospheric disturbances gradually develop following the flare onset and reach the highest level approximately at 18:45 UT, about 2.5 hours after the flare peak. The significantly slower response is because of the time needed for neutrals to accumulate, dissipate, and redistribute the absorbed solar energy. Similar findings have been found in terrestrial flare-impact studies [e.g., *Liu et al.*, 2007; *Pawlowski and Ridley*, 2008], showing that there is no apparent one-to-one correspondence between solar inputs and upper atmospheric states. Instead, the integral of solar radiation over a time history is more important than instantaneous irradiance. This poses the difficulty of attributing neutral perturbations to solar irradiance at a specific time point.

The other difference between the ionospheric and atmospheric responses is on the perturbation domain and magnitude. Our results suggest that the ionospheric electron density may increase substantially by up to an order of magnitude in this flare event, mostly concentrated at low altitudes of ~55-105 km (with the maximum percentage increase at ~70 km). Note that the electron concentration in this region (where photoionization is from solar X-rays) is orders of magnitude lower than that in the main ionospheric layer (which is typically above 120 km with photoionization mainly from solar EUV). Figure 2 shows that the main ionospheric density enhancement is indeed moderate: up to 25% near 210 km altitude. For the neutral upper atmosphere, its perturbations are concentrated at high altitudes (mostly above 150 km), and the percentage increase grows with increasing altitude. Within the MGITM spatial domain of <300 km altitude, the maximum flare-induced changes in the dayside-averaged properties are 7% for the neutral temperature,

46% for the thermal pressure, 122%, 34%, 73%, and 66% for the densities of CO_2, O, CO, and N_2, respectively. Due to the different increase in O and CO_2, their density ratio is reduced by up to −40% in the event. The high-altitude concentration of the atmospheric effects can be explained by the fact that solar EUV heating dominates at high altitudes and quickly drops below ~160 km [e.g., *Bougher and Dickinson*, 1988]. The predicted perturbation amplitudes are consistent with the enhancement of EUV inputs (see the Supporting Information). However, the real impact in the exosphere (above 200 km) would probably have been greater, where an underestimation of the model is implied by Figure 1. Moreover, because MGITM uses a single temperature to approximate the bulk behavior of atmospheric species, the actual heating effect on some species could be greater than our prediction here [*Elrod et al.*, 2018].

In Figure 2i, we assess the upper atmospheric movement during the flare event by evaluating the altitude change (in units of km) of fixed pressure levels between the MGITM non-flare and flare cases. The pressure levels of 10^{-8} Pa, 10^{-5} Pa, and 10^{-2} Pa are located near the altitudes of 260 km, 135 km, and 86 km, respectively, at 09-10/15:00 in the non-flare case. Given that the pressure is a proxy of the atmospheric column mass, Figure 2i illustrates that the solar flare results in a significant upwelling in the dayside Martian atmosphere. At the time of the atmospheric disturbance peak (18:45 UT), the vertical expansion ranges from ~1 km near 135 km altitude to ~10 km near 260 km altitude. The upper atmospheric upwelling is consistent with the increase of the neutral species abundances at high altitudes (Figures 2d-2g) and also explains the ionospheric density enhancement there (Figure 2a). The ionospheric intensification at low altitudes (<110 km) is caused by the enhanced solar ionizing fluxes in the flare event, specifically in hard and soft X-ray wavelengths. The ionospheric density increase at high altitudes (>150 km), however, needs a careful examination. Its increase during the main flare burst directly results from the irradiance enhancement in the EUV range. On the other hand, the remarkable increase, which lasts >8 hours with the maximum amplitude reached hours after the flare peak, indicates an indirect effect. Because a photochemical equilibrium approximation is taken for the ionosphere in MGITM, the high-altitude ionospheric enhancement during the flare recovery phase must be caused by the atmospheric expansion, which brings more neutral species to high altitudes and leads to more local solar ionizing energy absorption. It is realized that the calculated ionospheric results as presented here are subject to model limitations due to the neglect of transport effects (whose importance starts to

8

increase above ~180 km altitude). This study focuses more on the understanding of neutral disturbances, and a more accurate modeling of the ionosphere could be included in a future work using a magnetohydrodynamic approach.

Figure 3 shows the horizontal distributions of the flare-induced atmospheric perturbations at 191.25 km altitude, as a function of MSO latitude and local time. We select four representative time points to examine the percentage differences between the MGITM non-flare and flare cases: 2017-09-10/16:15 (approximately flare peak), 2017-09-10/18:45 (approximately atmospheric perturbation peak), 2017-09-11/00:00 and 2017-09-11/05:00 (in the recovery tail, ~8 hours and ~13 hours after the flare peak, respectively). These horizontal variations provide supplemental information to the dayside-averaged altitude profile examination as conducted in Figure 2. It is illustrated that the upper atmospheric disturbances start and accumulate on the Sun-facing side in response to the flare impact, and at the same time propagate and diffuse into the nightside. The dayside perturbations demonstrate a general SZA dependence, although a dawn-dusk asymmetry exists with the maximum percentage increase in the morning sector. In the late recovery phase, while the dayside disturbances have mostly subsided, some residual changes are seen on the nightside. These results underscore the complexity of the upper atmospheric responses to solar flares, on both temporal and spatial variations.

4 Summary and Discussion

In this study we use the MGITM model to perform a global, time-dependent numerical simulation of the Mars upper atmospheric and ionospheric responses to the X8.2-class solar flare eruption during 10 September 2017. The flare irradiance for driving the model, covering a broad wavelength range of 0-190 nm at 1-minute time cadence, is specified by a spectral irradiance model using both in-situ MAVEN EUVM measurements and Earth measurements for improved accuracy. By comparing two time-dependent runs for the non-flare and flare scenarios, we find that the solar flare results in instantaneous intensification in the dayside ionospheric electron density, most pronounced at altitudes lower than ~110 km due to the dominance of the flare enhancement at the short-wavelength end of the spectrum. There is a close correlation between the changes of electron densities and solar ionizing fluxes in both perturbation magnitude and in time scale. In contrast, the solar flare effectiveness in the neutral atmosphere proceeds through accumulation and redistribution processes on the Sun-facing side, with the maximum perturbations

reached about 2.5 hours after the flare peak. Our model results predict a remarkable increase in neutral species abundances: by up to 122%, 73%, 66%, and 34% for CO_2, CO, N_2, and O, respectively. The neutral atmospheric disturbance is primarily concentrated at altitudes higher than ~150 km, generally increasing its amplitude with rising altitude. In accordance with the flare-induced atmospheric upwelling due to solar EUV heating (ranging from an upward movement of ~1 km at 135 km altitude to ~10 km at 260 km), the high-altitude ionosphere during the recovery phase of the flare is subject to a moderate increase of up to 25% at ~210 km altitude through the photoionization increase. It is also shown that the dayside atmospheric disturbance propagates and diffuses into the nightside. It takes the Mars system more than 12 hours past the flare peak to generally recover to pre-flare levels.

The MGITM results have been compared with MAVEN in-situ measurements along spacecraft periapsis passages. While the comparison with the MAVEN data suggests that the model may have underestimated the solar flare impact at high altitudes, the general model-data agreement is satisfactory. The atmospheric density perturbations are reasonably captured during the flare and the subsequent recovery, on both spatial and temporal scales. There are two noteworthy advantages of the modeling approach to satellite observations. First, not limited to the investigation of the atmospheric time sequence during the flare event, our numerical study enables retrieval of net flare effects. By subtracting the MGITM results of the non-flare (pseudo) case from those of the flare (realistic) case, we effectively minimize the impact of the current modeling challenge in replicating all the details of satellite-observed atmospheric states. Furthermore, we mitigate the interference from other variability sources that are implicitly included in orbit-to-orbit changes, such as longitudinal effects. Our results reflect our best understanding of the Mars system's response solely to the solar flare, which stems from our current understanding of upper atmospheric physical processes that are included in the model. The general validity of the model has been confirmed [*Bougher et al.*, 2015a,b]. Second, the flare disturbance is assessed in a spatially global and temporally continuous manner. As a comparison, in-situ data have very limited spatial and temporal coverages. This work represents the first numerical attempt to realistically simulate the Mars upper atmospheric responses to a real solar flare event and to make direct model-data comparisons for the resulting perturbations. It is illustrated that the neutral regime is not exempt from the influence by space weather events, including solar flares (this work) and interplanetary coronal mass ejections

[*Fang et al.*, 2013]. It is of great science interest to explore in the future whether and how flare-induced perturbations in the upper atmosphere and ionosphere could propagate upward to the magnetosphere through coupling processes, particularly during stronger solar flares.

It is suggested that the processes that shape the Mars upper atmosphere during and after a solar flare are similar to those processes at Earth. Terrestrial studies have shown that solar flares result in atmospheric expansion and thermospheric density increases [e.g., *Liu et al.*, 2007; *Pawlowski and Ridley*, 2008; *Qian et al.*, 2011] and that the atmosphere slowly returns to the pre-flare state after dissipating the absorbed solar flare energy [*Pawlowski and Ridley*, 2011]. Despite the similarities, at Mars there are differences that play a role in modifying how its upper atmosphere responds to a flare event. For example, *Pawlowski and Ridley* [2008] simulated the response of the terrestrial upper atmosphere to a stronger X17 flare but found much weaker responses (in terms of percent changes) than what we present here for the relatively weaker X8.2 flare at Mars. This is not obvious because solar forcing at Mars may otherwise be thought to play a less significant role in driving thermospheric disturbances due to the longer distance to the Sun [*Bougher et al.*, 2015a]. Nevertheless, the thermospheric response is driven not only by the absorption of solar X-ray and EUV photons, but also by the efficiency of energy redistribution and dissipation. The dominant energy loss mechanisms at Mars (i.e., thermal conduction and CO_2 cooling) turn out to be less effective at removing the excess energy than at Earth (where O and NO cooling are important), besides the fact that the Martian atmosphere is much more tenuous than the terrestrial atmosphere. To further investigate the differences that the heating and cooling processes play at their respective planets, it would be helpful to conduct a comparative study for a same solar flare event. Such an investigation is the topic of future work.

References

Benna, M., P. R. Mahaffy, J. M. Grebowsky, J. L. Fox, R. V. Yelle, and B. M. Jakosky (2015), First measurements of composition and dynamics of the Martian ionosphere by MAVEN's Neutral Gas and Ion Mass Spectrometer, *Geophys. Res. Lett., 42*, doi:10.1002/2015GL066146.

Bougher, S. W. and R. E. Dickinson (1988), Mars mesosphere and thermosphere: 1. Global mean heat budget and thermal structure, *J. Geophys. Res., 93(A7)*, 7325-7337.

Bougher, S. W., S. Engel, R. G. Roble, and B. Foster (2000), Comparative terrestrial planet thermospheres: 3. Solar cycle variation of global structure and winds at solstices, *J. Geophys. Res., 105(E7)*, 17669-17692, doi:10.1029/1999JE001232.

Bougher, S. W., D. Pawlowski, J. M. Bell, S. Nelli, T. McDunn, J. R. Murphy, M. Chizek, and A. Ridley (2015a), Mars Global Ionosphere-Thermosphere Model: Solar cycle, seasonal, and diurnal variations of the Mars upper atmosphere, *J. Geophys. Res. Planets, 120*, 311-342. doi:10.1002/2014JE004715.

Bougher, S. W., et al. (2015b), Early MAVEN Deep Dip campaign reveals thermosphere and ionosphere variability, *Science, 350*, 0459, doi:10.1126/science.aad0459.

Bougher, S. W., et al. (2017), The structure and variability of Mars dayside thermosphere from MAVEN NGIMS and IUVS measurements: Seasonal and solar activity trends in scale heights and temperatures, *J. Geophys. Res. Space Physics, 122*, 1296-1313, doi:10.1002/2016JA023454.

Elrod, M. K., Curry, S. M., Thiemann, E. M. B., & Jain, S. K. (2018). September 2017 solar flare event: Rapid heating of the Martian neutral upper atmosphere from the XâĂŘclass flare as observed by MAVEN. *Geophysical Research Letters*, 45, 8803âĂŞ 8810. https://doi.org/10.1029/2018GL077729.

Eparvier, F., P. Chamberlin, T. Woods, and E. Thiemann (2015), The solar extreme ultraviolet monitor for MAVEN, *Space Sci. Rev.*, doi:10.1007/s11214-015-0195-2.

Fallows, K., P. Withers, and G. Gonzalez (2015), Response of the Mars ionosphere to solar flares: Analysis of MGS radio occultation data, *J. Geophys. Res. Space Physics, 120*, 9805-9825, doi:10.1002/2015JA021108.

Fang, X., S. W. Bougher, R. E. Johnson, J. G. Luhmann, Y. Ma, Y.-C. Wang, and M. W. Liemohn (2013), The importance of pickup oxygen ion precipitation to the Mars upper atmosphere under extreme solar wind conditions, *Geophys. Res. Lett., 40*, 1922-1927, doi:10.1002/grl.50415.

Fang, X., Y. Ma, D. Brain, Y. Dong, and R. Lillis (2015), Control of Mars global atmospheric loss by the continuous rotation of the crustal magnetic field: A time-dependent MHD study, *J. Geophys. Res. Space Physics, 120*, 10,926-10,944, doi:10.1002/2015JA021605.

Fang, X., et al. (2017), The Mars crustal magnetic field control of plasma boundary locations and atmospheric loss: MHD prediction and comparison with MAVEN, *J. Geophys. Res. Space Physics, 122*, doi:10.1002/2016JA023509.

Gurnett, D. A., D., Kirchner, R. Huff, D. Morgan, A. Persoon, T. Averkamp, F. Duru, E. Nielsen, E., A. Safaeinili, J. Plaut, and G. Picardi (2005), Radar soundings of the ionosphere of Mars, *Science, 310*, 1999-1933.

Haider, S. A., M. A. Abdu, I. S. Batista, J. H. Sobral, E. Kallio, W. C. Maguire, and M. I. Verigin (2009), On the responses to solar X-ray flare and coronal mass ejection in the ionospheres of Mars and Earth, *Geophys. Res. Lett., 36*, L13104, doi:10.1029/2009GL038694.

Haider, S. A., S. M. P. McKenna-Lawlor, C. D. Fry, R. Jain, and K. N. Joshipura (2012), Effects of solar X-ray flares in the E region ionosphere of Mars: First model results, *J. Geophys. Res., 117*, A05326, doi:10.1029/2011JA017436.

Jakosky, B., et al. (2015), The Mars Atmosphere and Volatile Evolution (MAVEN) Mission. *Space Sci. Rev.*, doi:10.1007/s11214-015-0139-x.

Lee, C. O., Jakosky, B. M., Luhmann, J. G., Brain, D. A., Mays, M. L., Hassler, D. M., et al. (2018). Observations and impacts of the 10 September 2017 solar events at Mars: An overview and synthesis of the initial results. *Geophysical Research Letters*, 45, 8871-8885. https://doi.org/10.1029/2018GL079162

Liu, H., H. Luhr, S. Watanabe, W. Kohler, and C. Manoj (2007), Contrasting behavior of the thermosphere and ionosphere in response to the 28 October 2003 solar flare, *J. Geophys. Res., 112*, A07305, doi:10.1029/2007JA012313.

Lollo, A., P. Withers, K. Fallows, Z. Girazian, M. Matta, and P. C. Chamberlin (2012), Numerical simulations of the ionosphere of Mars during a solar flare, *J. Geophys. Res., 117*, A05314, doi:10.1029/2011JA017399.

Mahaffy, P., et al. (2014) The Neutral Gas and Ion Mass Spectrometer on the Mars Atmosphere and Volatile Evolution Mission, *Space Sci. Rev.*, DOI:10.1007/s11214-014-0091-1.

Mahaffy, P. R., M. Benna, M. Elrod, R. V. Yelle, S. W. Bougher, S. W. Stone, and B. M. Jakosky (2015), Structure and composition of the neutral upper atmosphere of Mars from the MAVEN NGIMS investigation, *Geophys. Res. Lett., 42*, doi:10.1002/2015GL065329.

Mahajan, K. K., Neelesh, K. Lodhi, and S. Singh (2009), Ionospheric effects of solar flares at Mars, *Geophys. Res. Lett., 36*, L15207, doi:10.1029/2009GL039454

Mendillo, M., P. Withwers, D. Hinson, H. Rishbeth, and B. Reinisch (2006), Effects of solar flares on the ionosphere of Mars, *Science, 311*, 1135-1138.

Nielsen, E., H. Zou, D. A. Gurnett, D. L. Kirchner, D. D.Morgan, R. Huff, R. Orosei, A. Safaeinili, J. J. Plaut, and G. Picardi (2006), Observations of vertical reflections from the topside Martian ionosphere, *Space Sci. Rev., 126*, 373-388, doi:10.1007/s11214-006-9113-y.

Pawlowski, D., and A. Ridley (2008), Modeling the thermospheric response to solar flares, *J. Geophys. Res., 113*, A10, 309, doi:10.1029/2008JA013182.

Pawlowski, D., and A. Ridley (2011), The effects of different solar flare characteristics on the global thermosphere, *J. Atmos. Terr. Phys., 73*, 1840-1848, doi:10.1016/j.jastp.2011.04.004.

Putzig, N. E., Mellon, M. T., Kretke, K. A., & Arvidson, R. E. (2005). Global thermal inertia and surface properties of Mars from the MGS mapping mission. *Icarus*, 173(2), 325âĂŞ341. https://doi.org/10.1016/j.icarus.2004.08.017

Qian, L., Burns, A. G., Chamberlin, P. C., and Solomon, S. C. (2011), Variability of thermosphere and ionosphere responses to solar flares, *J. Geophys. Res.*, 116, A10309, doi:10.1029/2011JA016777.

Ridley, A., Y. Deng, and G. Toth (2006), The Global Ionosphere-Thermosphere Model, *J. Atmos. Sol. Terr. Phys., 68*, 839-864.

Thiemann, E. M. B., F. G. Eparvier, L. A. Andersson, C. M. Fowler, W. K. Peterson, P. R. Mahaffy, S. L. England, D. E. Larson, D. Y. Lo, N. M. Schneider, et al. (2015), Neutral density response to solar flares at Mars, *Geophys. Res. Lett., 42*, 8986-8992, doi:10.1002/2015GL066334.

Thiemann, E. M. B., P. C. Chamberlin, F. G. Eparvier, B. Templeman, T. N. Woods, S. W. Bougher, B. M. Jakosky (2017), The MAVEN EUVM model of solar spectral irradiance variability at Mars: Algorithms and results, *J. Geophys. Res. Space Physics, 122*, 2748-2767, doi:10.1002/2016JA023512.

Thiemann, E. M. B., Andersson, L., Lillis, R., Withers, P., Xu, S., Elrod, M., et al. (2018). The Mars topside ionosphere response to the X8.2 solar flare of 10 September 2017. *Geophysical Research Letters*, 45, 8005âĂŞ8013. https://doi.org/10.1029/2018GL077730.

Xu, S., Thiemann, E., Mitchell, D., Eparvier, F., Pawlowski, D., Benna, M., al., et (2018). Observations and modeling of the Mars lowâĂŘaltitude ionospheric response to the 10 September 2017 XâĂŘClass solar flare. *Geophysical Research Letters*, 45, 7382-7390. https://doi.org/10.1029/2018GL078524

Zurek, R. W., R. A. Tolson, S. W. Bougher, R. A. Lugo, D. T. Baird, J. M. Bell, and B. M. Jakosky (2017), Mars thermosphere as seen in MAVEN accelerometer data, *J. Geophys. Res. Space Physics, 122*, doi:10.1002/2016JA023641.
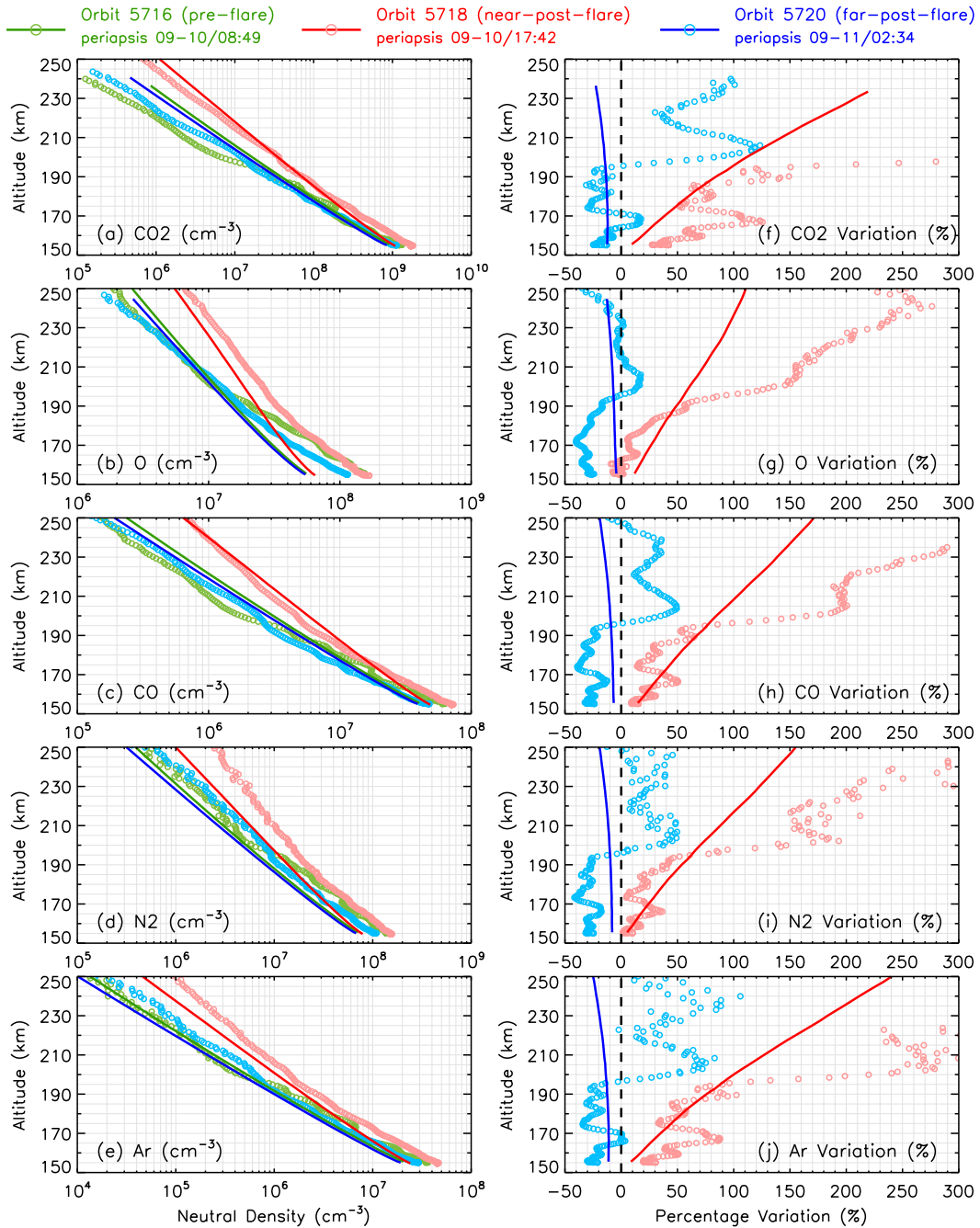
Figure 1. Comparison of the MGITM calculated CO_2, O, CO, N_2, and Ar neutral densities with MAVEN NGIMS in-situ measurements along MAVEN pre-flare (green), near-post-flare (red), and far-post-flare (blue) orbits during the 10 September 2017 solar flare event. Figures 1a-1e present the neutral species abundances, and Figures 1f-1j present the percentage differences along the two post-flare orbits relative to the pre-flare orbit. The model results and MAVEN data are indicated by solid lines and open circles, respectively.
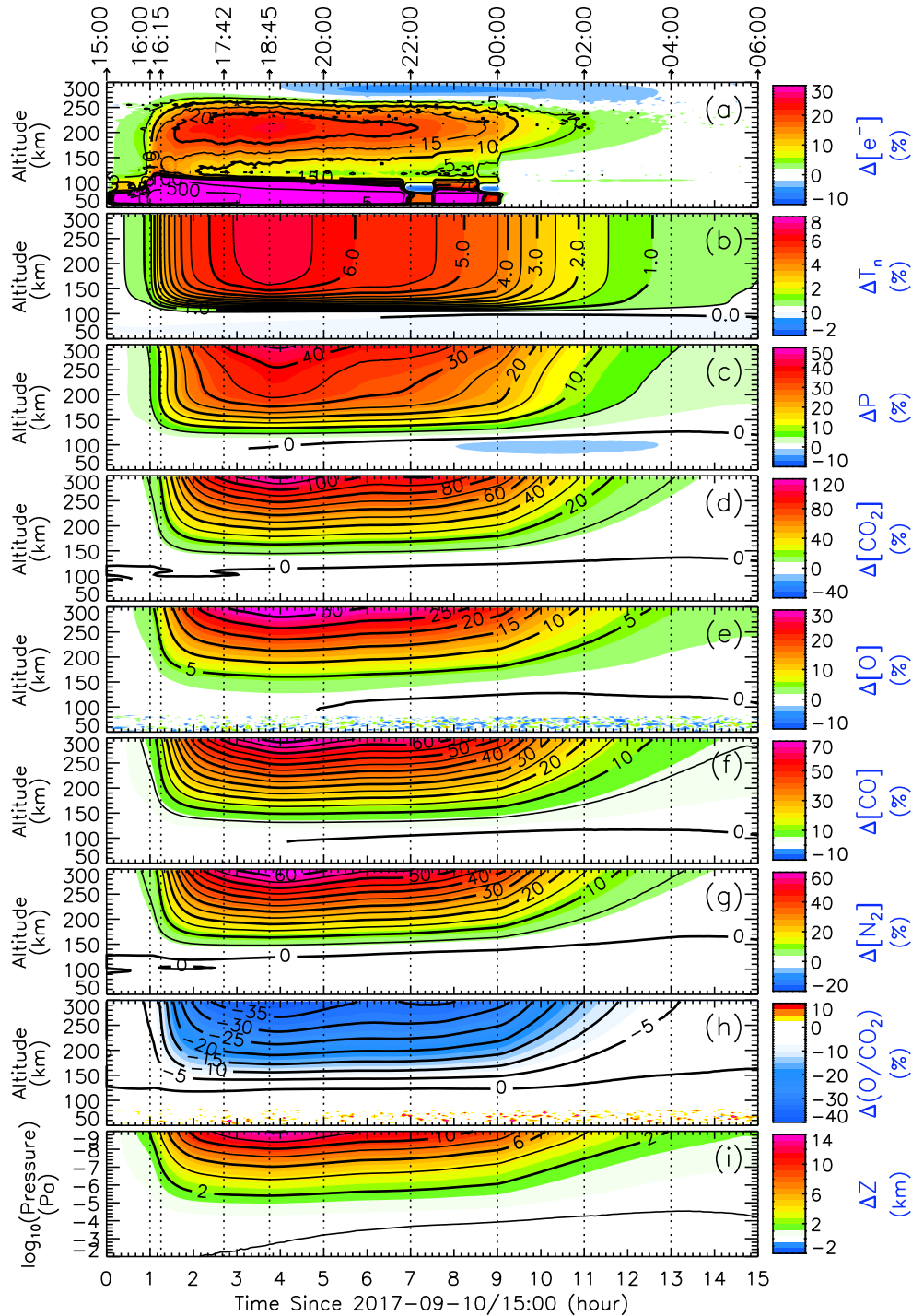
Figure 2. MGITM average dayside upper atmospheric perturbations, beginning from 2017-09-10/15:00:00, ~1 hour prior to the flare onset. Here are shown the time-varying percentage changes of the dayside-averaged altitude profiles (SZA<90°) in the flare case compared with the non-flare case for (a) electron density, (b) neutral temperature, (c) thermal pressure, (d) CO_2 density, (e) O density, (f) CO density, (g) N_2 density, and (h) number density ratio of O to CO_2. Figure 2i shows the altitude difference in units of km between the pressure levels in the two cases. Note that the order of pressure on the vertical axis of Figure 2i has been reversed to make altitude increase from the bottom to the top of the panel. In all the panels, we use green-red colors to denote positive changes and use blue for negative changes. As denoted above the top panel, we mark the following representative time points: 16:00 (flare onset), 16:15 (approximately flare peak), 17:42 (MAVEN periapsis passage), and 18:45 (approximately neutral response peak). We also mark time points in the recovery phase at a time interval of 2 hours.
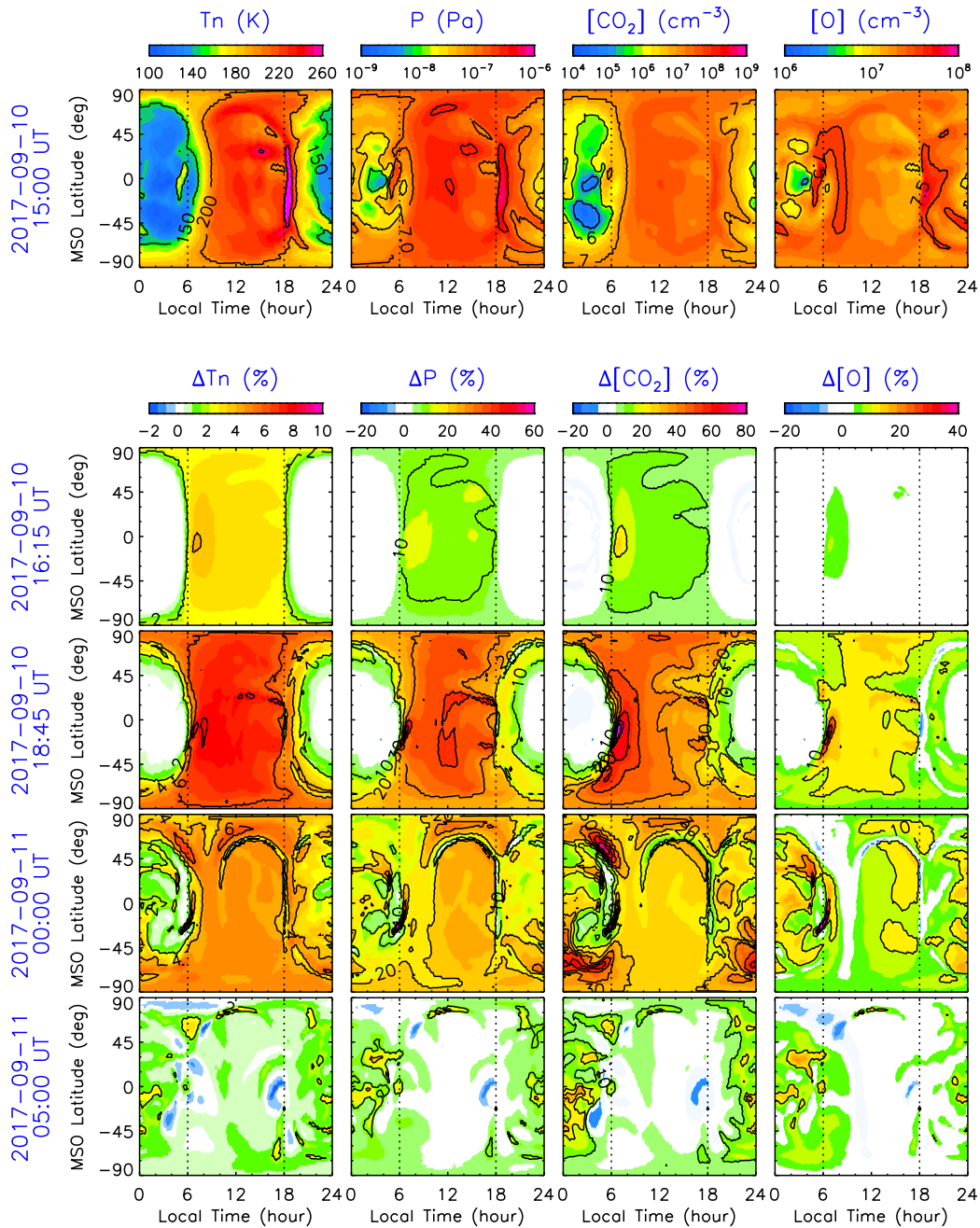
Figure 3. The top row shows the MGITM-calculated horizontal distributions of (from left to right) neutral temperature, thermal pressure, CO_2 and O number densities at 191.25 km altitude prior to the flare onset at 2017-09-10/15:00. The results are shown in MSO latitude and local time, with the subsolar point located in the panel center. The subsequent four rows show the percentage differences between the non-flare case and the flare case at four representative time points: 2017-09-10/16:15, 2017-09-10/18:45, 2017-09-11/00:00, and 2017-09-11/05:00, respectively.

Figure 1.
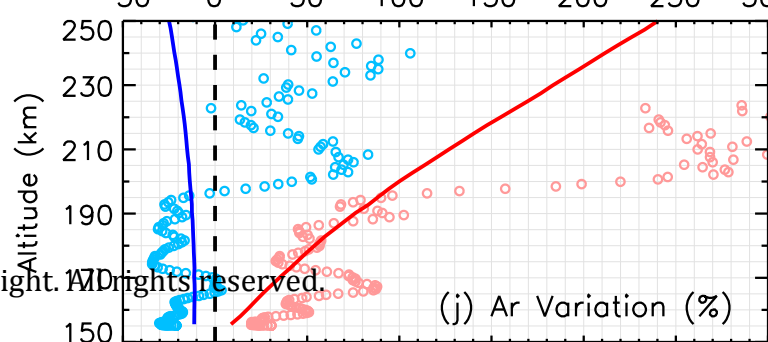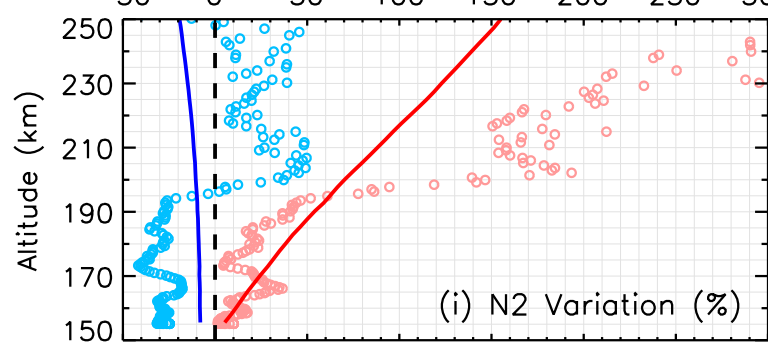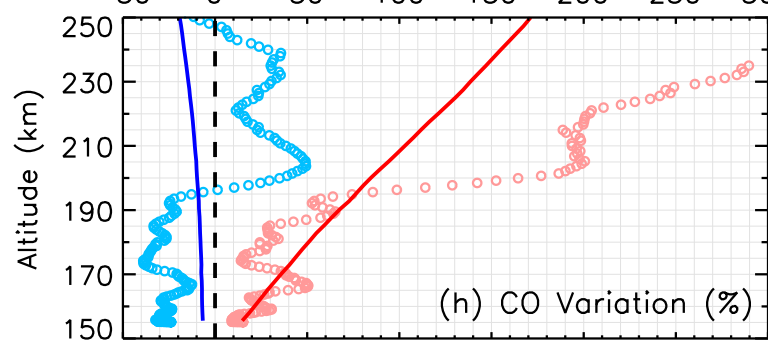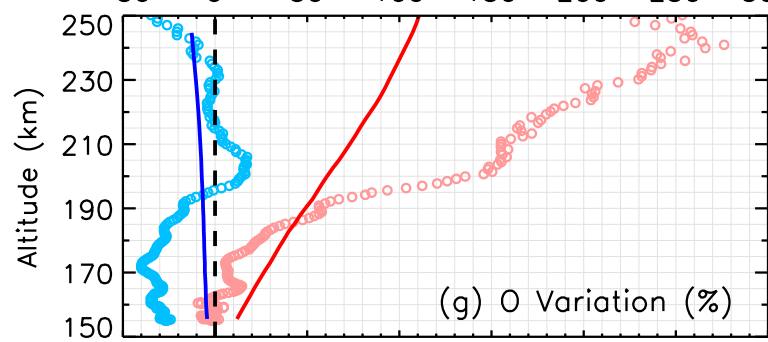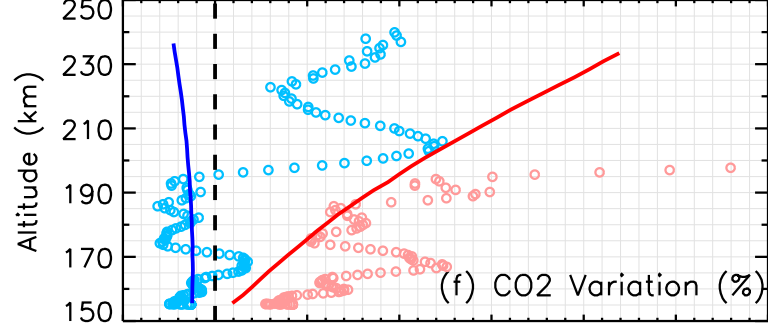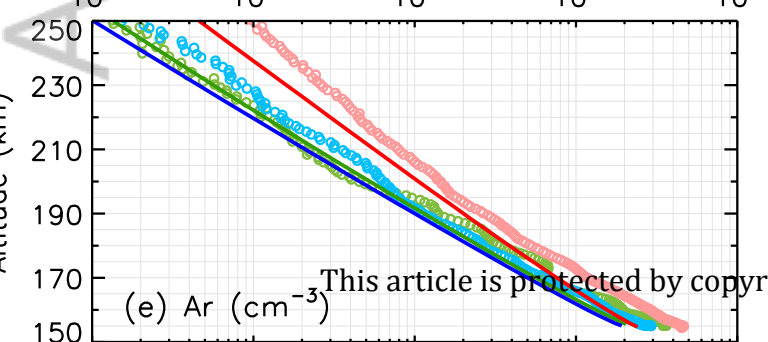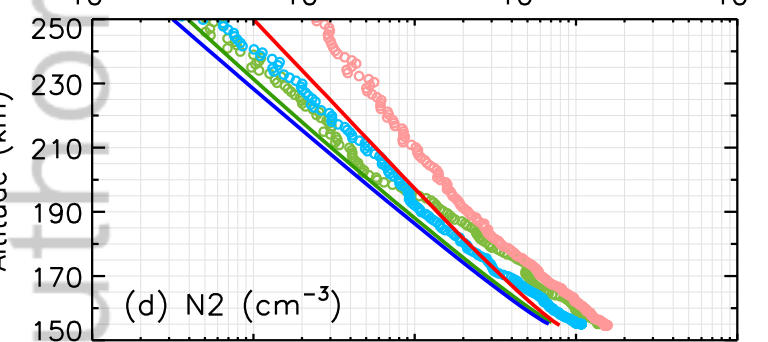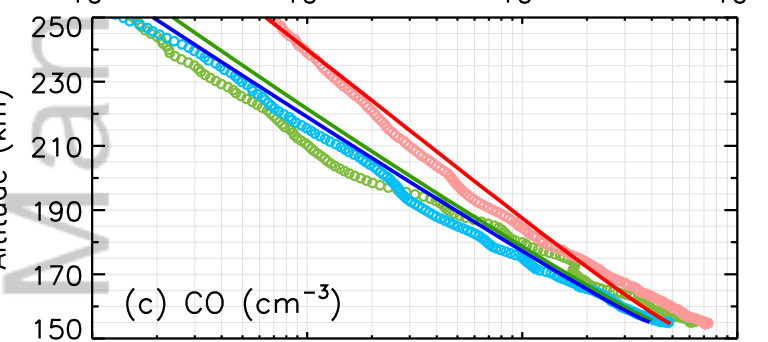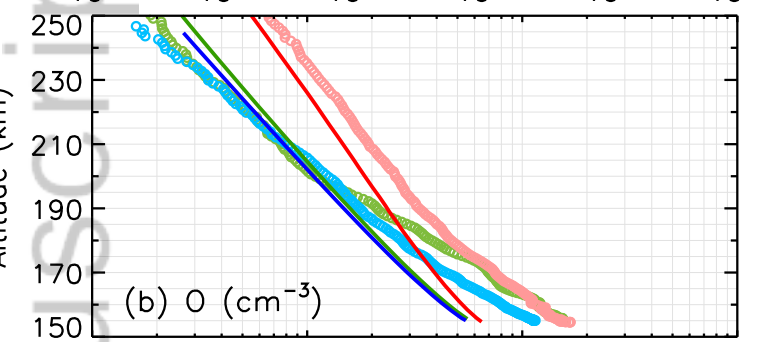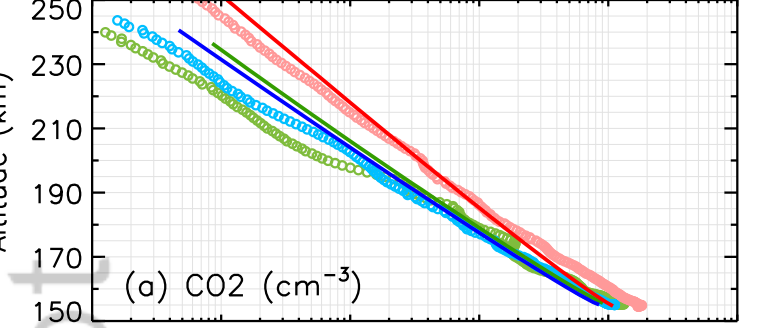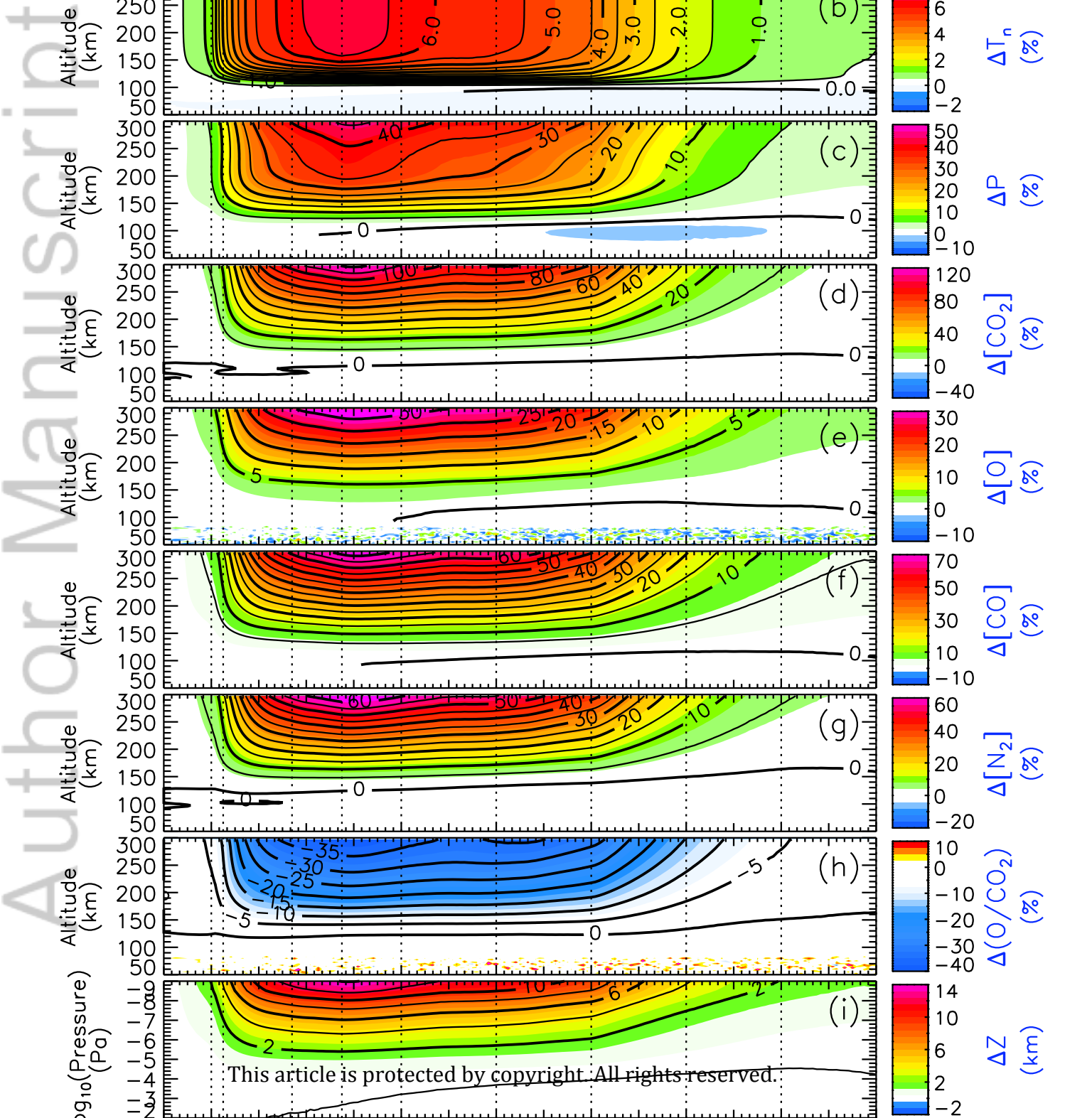
Figure 2.

Figure 3.

ΔTn (%)   ΔP (%)   Δ[CO₂] (%)   Δ[O] (%)

(a) CO2 (cm^{-3})

(b) O (cm^{-3})

(c) CO (cm^{-3})

(d) N2 (cm^{-3})

(e) Ar (cm^{-3})

(f) CO2 Variation (%)

(g) O Variation (%)

(h) CO Variation (%)
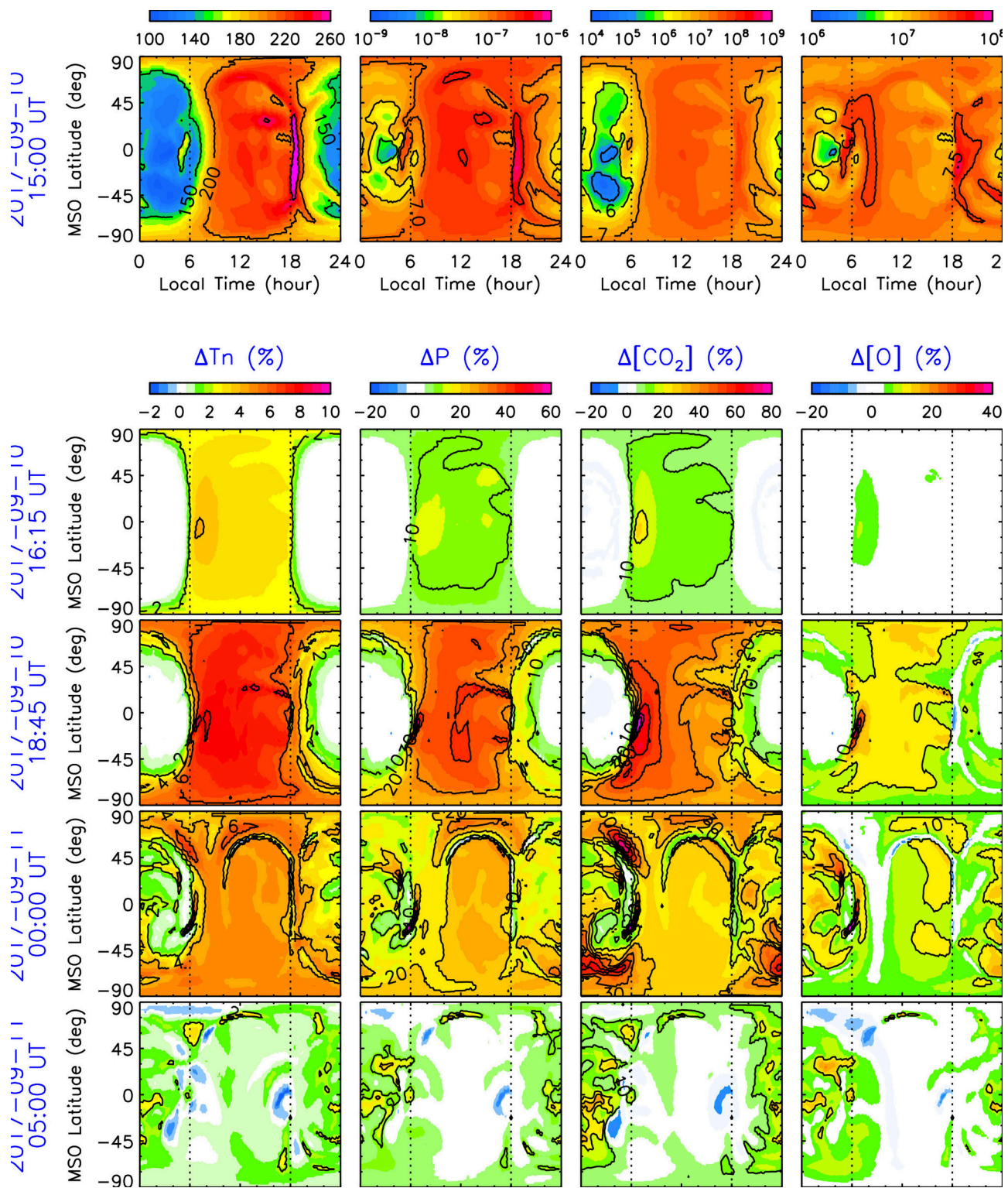
(i) N2 Variation (%)

(j) Ar Variation (%)

Altitude (km)
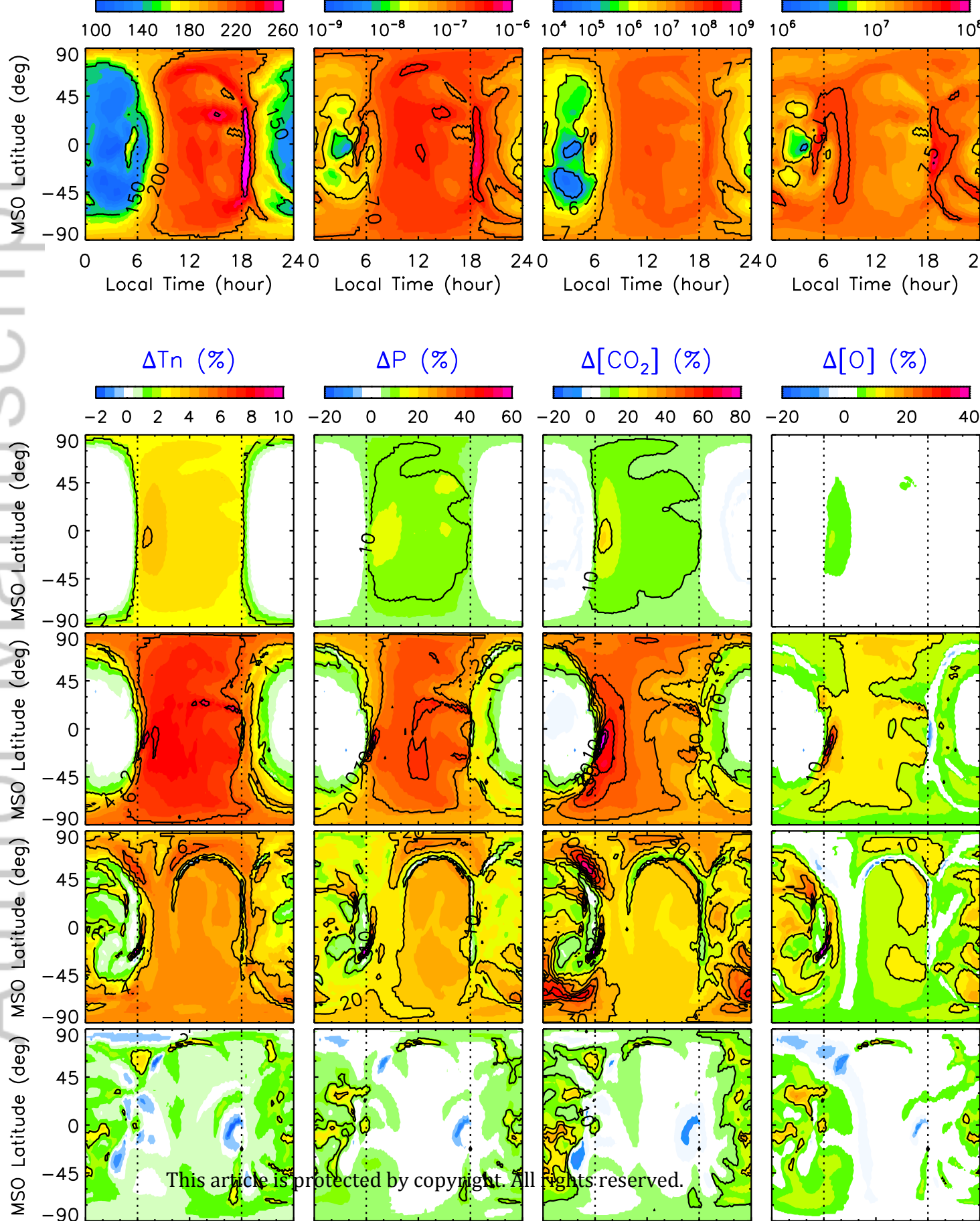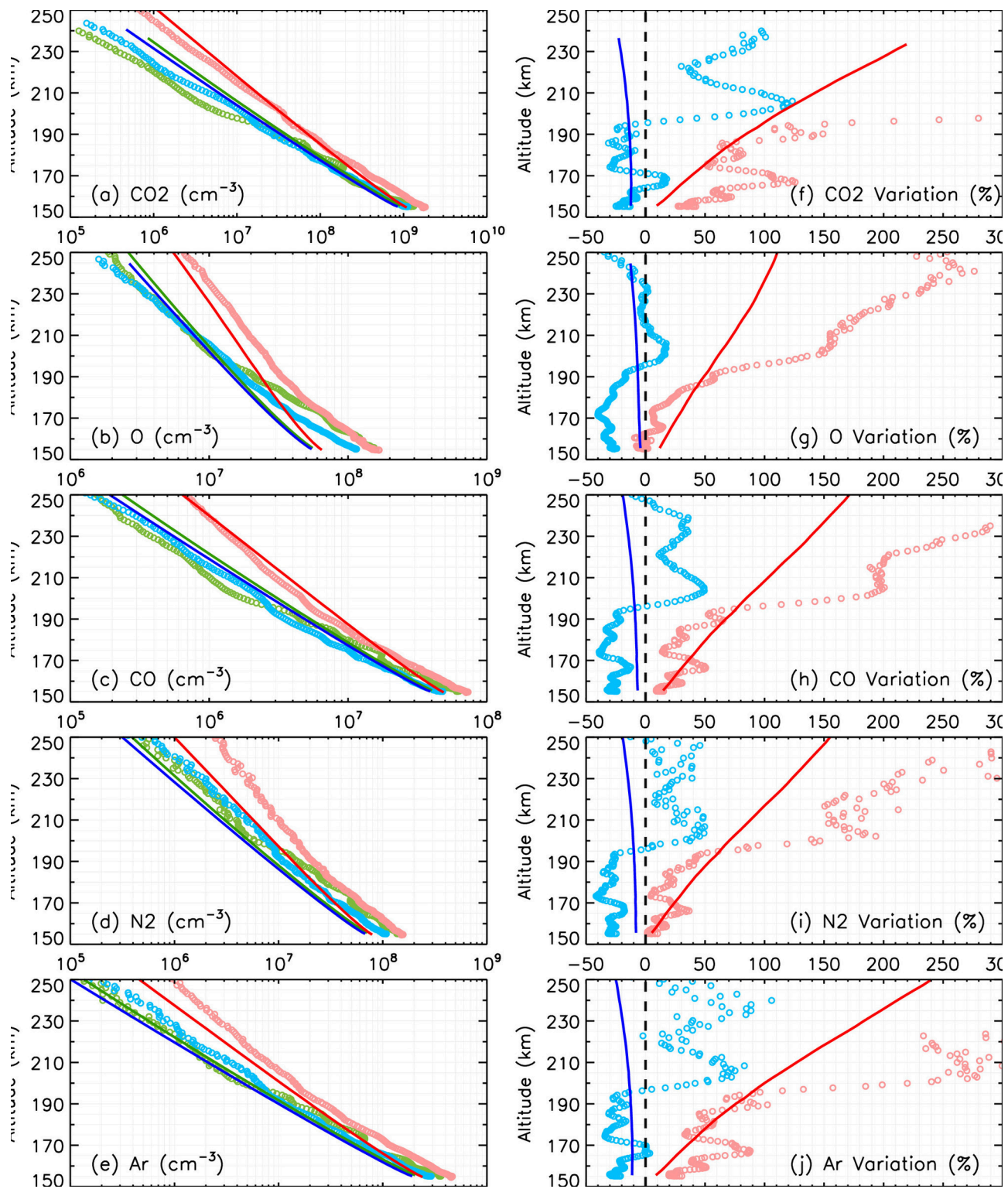
2019gl084515-f01-z-.eps
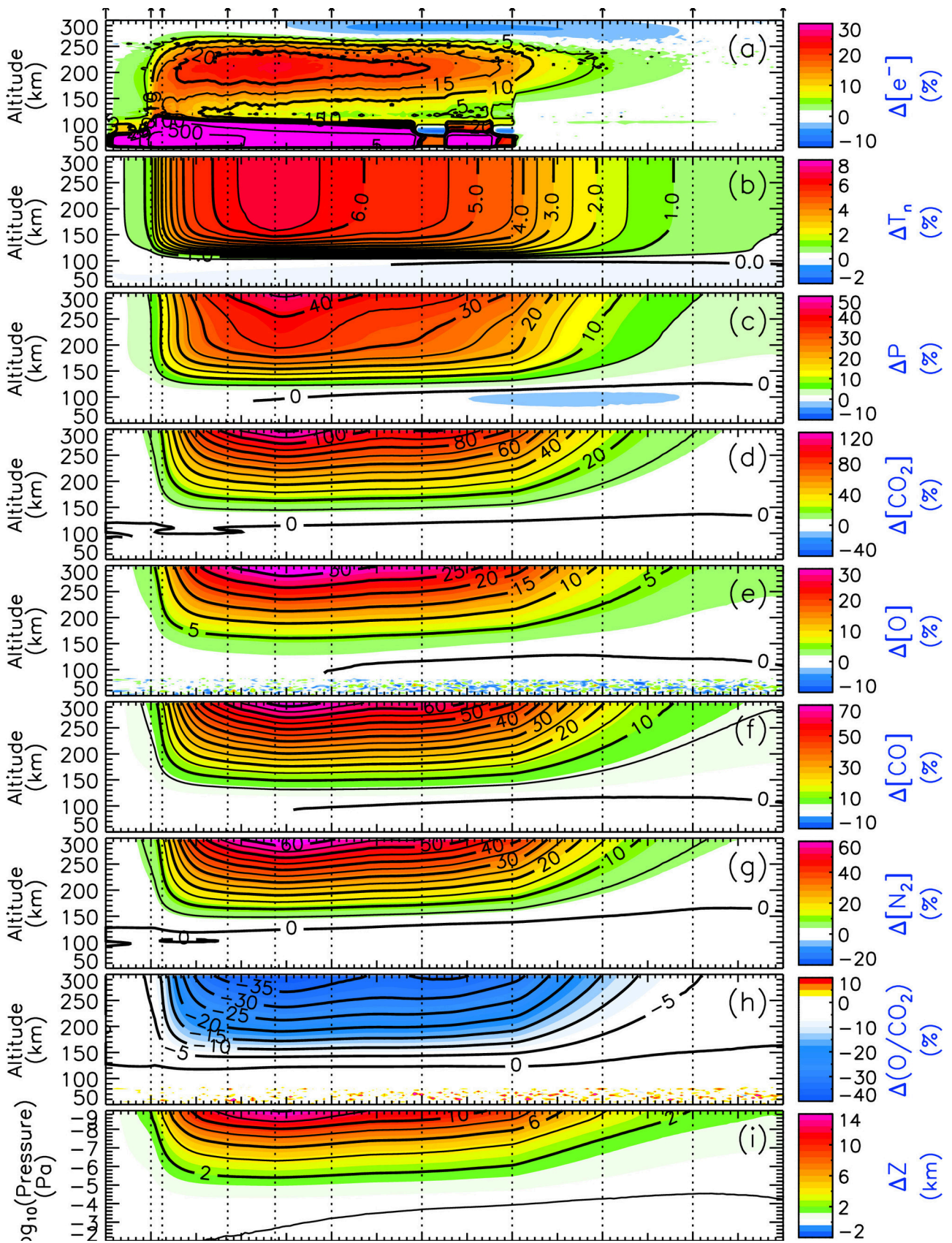
2019gl084515-f02-z-.eps

2019gl084515-f03-z-.eps